Nanoscale

PAPER

Published on 22 May 2025
Licence and permissions

Cite this: *Nanoscale*, 2025, **17**, 14660

Physicochemical characterization of a new porous 2D semiconductor carbon allotrope, C_{16}: an investigation *via* density functional theory and machine learning-based molecular dynamics†

K. A. L. Lima,[a] R. A. F. Alves,[b,c] E. A. Moujaes,[d] A. C. Dias,[b,e] D. S. Galvão,[a] M. L. Pereira, Jr[f] and Luiz A. Ribeiro, Jr *[b,c]

This study comprehensively characterizes, with suggested applications, a novel two-dimensional carbon allotrope, C_{16}, using density functional theory and machine learning-based molecular dynamics. This nanomaterial is derived from naphthalene and bicyclopropylidene molecules, forming a planar configuration with sp^2 hybridization and featuring 3-, 4-, 6-, 8-, and 10-membered rings. The cohesive energy of −7.1 eV per atom, the absence of imaginary frequencies in the phonon spectrum, and the retention of the system's topology after *ab initio* molecular dynamics simulations confirm the structural stability of C_{16}. The nanomaterial exhibits a semiconducting behavior with a direct band gap of 0.59 eV and anisotropic optical absorption in the *y* direction. Assuming a complete absorption of incident light, it registers a power conversion efficiency of 13%, demonstrating relatively good potential for applications in solar energy conversion. Excluding the vacuum effect along the non-periodic *z* direction, the planar lattice thermal conductivity κ_L reaches ultralow values of 1.90×10^{-2} W (m K)$^{-1}$, 0.90×10^{-2}, and 0.59×10^{-2} for T = 300 K, 600 K, and 1000 K, respectively along both *x* and *y* directions. Very close to the Fermi level, the thermoelectric figure of merit (zT) can reach a maximum value of 0.93 at room temperatures along both planar directions, indicating an excellent ability to convert a temperature gradient into electrical power. Additionally, C_{16} demonstrates high mechanical strength, with Young's modulus values of 500 GPa and 630 GPa in the *x* and *y* directions, respectively. Insights into the electronic, optical, thermoelectric, and mechanical properties of C_{16} reveal its promising capability for energy conversion applications.

Received 27th March 2025,
Accepted 16th May 2025

DOI: 10.1039/d5nr01282a

rsc.li/nanoscale

1 Introduction

The fabrication of new nanomaterials has always been associated with technological progress. Advancing nanotechnology requires a deep understanding of nanomaterials.[1] Nanomaterials can exist at different dimensionalities, from zero (quantum dots) to three dimensions (such as diamonds). In particular, two-dimensional (2D) materials have recently attracted significant attention due to their properties and potential applications in various technological fields,[2] including electronics,[3] optoelectronics,[4] and energy storage.[5]

Since the experimental realization of graphene,[6] more than two decades ago, the investigation of new carbon allotropes and other 2D materials has been at the forefront of materials science. Graphene is a semimetal material[7] with high tensile strength[8] and elevated thermal stability.[9] These attractive properties have motivated the search for new materials with similar or improved properties.[10]

Among the growing number of 2D materials families, carbon allotropes are particularly promising due to carbon's ability to form multiple bonding configurations (sp, sp^2, and sp^3 hybridizations and combinations of them),[11] resulting in a large diversity of physical characteristics dependent on the structural topology of atomic arrangements.[12] Although graphene exhibits high electrical conductivity, it has a zero electronic bandgap, limiting some kinds of applications.[13] This

[a]*Department of Applied Physics and Center for Computational Engineering and Sciences, State University of Campinas, Campinas, São Paulo, 13083-859, Brazil*
[b]*Institute of Physics, University of Brasília, 70910-900 Brasília, Brazil. E-mail: ribeirojr@unb.br*
[c]*Computational Materials Laboratory, LCCMat, Institute of Physics, University of Brasília, 70910-900 Brasília, Brazil*
[d]*Institute of Physics, Department of Solid State Physics, Federal University of Bahia, Campus Ondina, 40170-115 Salvador, Brazil*
[e]*International Center of Physics, University of Brasília, Brasília, 70910-900, Brazil*
[f]*University of Brasília, College of Technology, Department of Electrical Engineering, Federal District, 70919-970 Brasília, Brazil*

† Electronic supplementary information (ESI) available: Structure (cif) file for the proposed material and results for complementary simulations. See DOI: https://doi.org/10.1039/d5nr01282a

limitation has stimulated research into new 2D carbon allotropes that combine graphene's structural benefits with semiconducting properties.[14]

This growing interest in carbon-based 2D systems has led to the discovery and/or proposal of several new allotropes with distinct characteristics. Although most of these structures are from theoretical predictions,[12,15–19] significant advances have recently been made in the synthesis routes of these nanomaterials.

In addition to graphene,[6] fullerenes,[20] and carbon nanotubes,[21] which were synthesized years ago, recent experimental realizations include biphenylene network (BPN),[22] holey graphyne (HGY),[23] γ-graphyne (γ-GY),[24–26] and monolayer fullerene network (2D-C_{60}).[27] These systems were theoretically predicted before they were synthesized.[28–31] Importantly, graphene and BPN exhibit metallic behavior, while the HGY, 2D-C_{60}, and γ-GY monolayers are semiconductors.

Among the previously proposed or experimentally realized two-dimensional porous carbon allotropes, such as phagraphene,[32] biphenylene networks,[22] and graphdiyne derivatives,[33] C_{16} stands out due to its unique construction from fused naphthalene and bicyclopropylidene motifs. This structural design leads to a periodic framework composed of 3-, 4-, 6-, 8-, and 10-membered carbon rings, an unprecedented combination among 2D carbon systems. While phagraphene and biphenylene networks exhibit metallic character, C_{16} displays semiconducting behavior with a direct band gap, making it a promising candidate for optoelectronic and thermoelectric applications. Thus, C_{16} enriches the structural diversity of two-dimensional carbon allotropes and introduces a novel porous semiconducting platform derived from an unconventional molecular fusion strategy.

In our quest to discover new 2D carbon allotropes, our groups have recently characterized 30 two-dimensional structures with semiconducting properties, specifically focusing on their solar energy conversion capabilities. Our results demonstrate that power conversion efficiency (PCE) values range from 7% to 30%, with the possibility of complete absorption of an incident light.[34] Beyond their main use in electronic devices, these 2D semiconducting carbon allotropes also appear to be promising candidates for renewable energy applications.[35]

In this context, this work proposes a new carbon allotrope named C_{16}. Density functional theory (DFT) simulations were employed to characterize the dynamical and thermal stability, electronic structure, and optical, excitonic, and thermoelectric properties of the material.

We have also performed classical molecular dynamics (MD) simulations to study its mechanical properties. For the description of interatomic interactions, we have employed a reactive force field trained using machine learning protocols based on data obtained from *ab initio* molecular dynamics (AIMD) simulations for representative structures related to C_{16}.

Our results show that C_{16} is dynamically and structurally stable, with no imaginary frequencies in its phonon spectrum. It is also thermally stable, as no phase changes were observed when subjected to a thermal bath at 1000 K. C_{16} exhibits a semiconducting behavior, with a direct electronic bandgap of 0.59 eV. Regarding its optical properties, C_{16} exhibits anisotropic characteristics, with the main absorption activity occurring along one specific direction of the system. It has an exciton binding energy of approximately 96 meV, a power conversion efficiency (PCE) of 13%, and a figure of merit of 0.8. Regarding its mechanical properties, our results suggest an anisotropic behavior, with Young's modulus ranging from 500 GPa to 630 GPa, depending on the direction of deformation.

2 Methodology

To better present the selected computational methods and simulation parameters, we have divided this section into three subsections: the modeling of C_{16}, the first-principles calculations, and the aspects of classical MD simulations.

2.1 System modeling

Different approaches can be taken to proposing new nanomaterials based on carbon or other systems. One common approach, also frequently used in experimental processes, is to start with known hydrocarbon molecular motifs and dehydrogenate them to induce reactions.

In the literature, several structures have been obtained through the process above. Examples include the BPN and 2D-C_{60} networks, which are obtained through the covalent bonding of BPN and C_{60} molecules, respectively.[22,27] For γ-GY, several small molecules can be used, particularly dehydrobenzoannulenes (DBAs).[36] This approach has been used for several proposed carbon monolayers, such as PAI-G,[37] PSI-G,[38] PCF,[39] naphthylene,[40] DHQ,[41] TH-GY,[42] nanoporous graphene,[43] among others.

In this perspective, here we propose a new allotrope, which consists of one possible 'fusion' of the naphthalene[44] and bicyclopropylidene[45] into a 2D structure that is also planar (like the molecules), see Fig. 1. The molecular motifs are shown in Fig. 1(a and b). Naphthalene is an oligoacene with ten carbons, with the formula $C_{10}H_8$, while bicyclopropylidene is a tetrasubstituted alkene with the formula C_6H_8.

The molecules were arranged in alternating linear blocks, forming covalent bonds. The system was designed to exhibit fully sp^2 hybridization. Fig. 1(c) shows a supercell of the system obtained from this process, with the molecular motifs highlighted in blue and green. The obtained structure (C_{16}) consists of carbon fused rings with 3, 4, 6, 8, and 10 atoms. The unit cell (rC_{16}) contains 16 carbon atoms, see the the bottom right panel of Fig. 1.

2.2 First-principles calculations

To characterize the physicochemical properties of C_{16}, we performed first-principles simulations using the DFT formalism within the Vienna *ab initio* simulation package (VASP).[46,47] The Kohn–Sham (KS) equations were solved *via* the projector augmented wave (PAW) method,[48] applying a plane-wave cutoff energy of 868.00 eV. We used the generalized gradient approximation (GGA) with the Perdew–Burke–Ernzerhof (PBE) exchange–correlation functional,[49] enforcing a convergence criterion of 0.01 eV $Å^{-1}$ for minimizing atomic forces and the stress tensor.

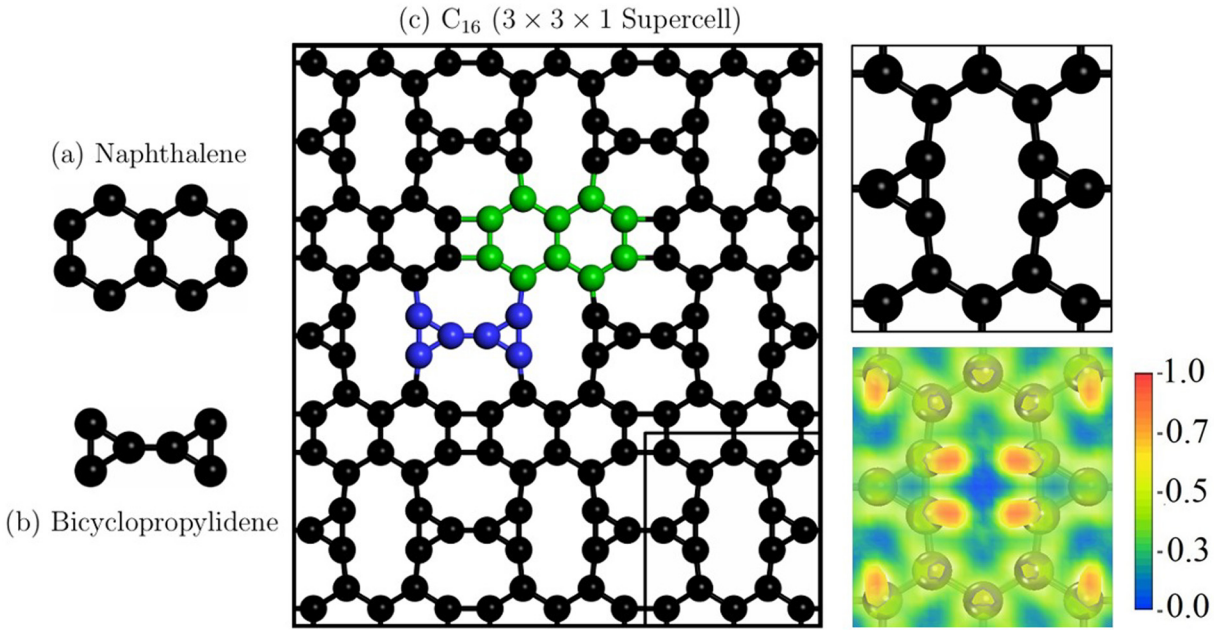

Fig. 1 Structural and electronic features of the proposed C_{16} carbon allotrope. (a) and (b) depict the molecular precursors used as structural inspiration: naphthalene and bicyclopropylidene. (c) shows a 3 × 3 × 1 supercell of C_{16} with the fused motifs highlighted – naphthalene-like units in green and bicyclopropylidene-like units in blue. The unit cell, marked in the bottom right of the supercell, contains only carbon atoms forming 3-, 4-, 6-, 8-, and 10-membered rings. The top right panel presents the atomic arrangement of the unit cell. In contrast, the bottom right panel displays the differential charge density distribution, where red and blue regions indicate charge accumulation and depletion, respectively.

After the geometry optimization (unit cell parameters and atomic positions), we obtained the C_{16} electronic properties with a cutoff energy of 488.23 eV adopting a total energy convergence criterion of 10^{-6} eV to ensure self-consistency in the electronic density. Due to systematic errors associated with the PBE functional in estimating the electronic bandgap value,[50,51] we applied the HSE06 hybrid exchange–correlation functional[52,53] for a more realistic estimation of the electronic and optical gaps. To avoid spurious interactions between the monolayer and its periodic images along the *z*-direction, a vacuum buffer space of 30 Å was used.

The plane-wave cutoff energy was set to 868.00 eV for the structural optimization stage, as determined by a convergence test that ensured total energy differences within 1 meV per atom and force convergence below 0.01 eV $Å^{-1}$. For the subsequent electronic structure calculations, a cutoff energy of 488.23 eV was used. This value is sufficient for the accurate evaluation of the band structure and density of states, given that the wavefunction and charge density were already converged in the previous step. Band gap variations remained below 0.01 eV when compared to higher cutoff values, confirming the adequacy of the chosen parameters.

In all calculations, the *k*-meshes were generated automatically using the Monkhorst–Pack method,[54] ensuring a density of 40 $Å^{-1}$ along the in-plane lattice vector directions,[55] which results in a 6 × 6 × 1 *k*-mesh for the unit cell. Dynamic stability was assessed by obtaining the phonon dispersion spectrum of a 3 × 3 × 1 supercell with 64 atoms, with the same convergence criteria mentioned above. To evaluate the thermal stability, we performed AIMD simulations under the canonical NVT ensemble, using a Nosé–Hoover thermostat[56] to control the temperature value set at 1000 K, with a time step of 1 fs for a total simulation time of 5 ps.

To investigate the excitonic and optical properties, we used a maximally localized Wannier function tight-binding (MLWF-TB)[57,58] Hamiltonian to solve the Bethe–Salpeter equation (BSE),[59] due to the high computational cost of GW + BSE *ab initio* approaches.[60,61] To determine MLWF-TB, through the Wannier90 code[57,62,63] we choose the C s- and p-orbital projections, based on the electronic density of states results, complemented with a random basis to achieve the same number of calculated bands in the DFT simulations.

The optical properties were analyzed at both the BSE level, which includes excitonic effects, and the independent particle approximation (IPA), which does not account for quasi-particle effects. These analyses were carried out using the WanTiBEXOS code.[58] The BSE was solved using a 2D-truncated Coulomb potential (V2DT)[64] and a *k*-mesh of 19 × 17 × 1; the highest two valence bands and the lowest three conduction bands were considered in the calculations to obtain an accurate description of the optical properties in the solar emission range (*i.e.* 0.5 eV to 4.0 eV). To ensure accurate results, we applied a smearing of 0.01 eV to the dielectric functions at both the BSE and IPA levels.

The thermoelectric properties, namely the Seebeck coefficient, electronic conductivity, and thermal conductivity, were computed using the Boltzmann code.[65] This tool is interfaced with the VASP code within the Wannier90 package and

depends on correctly producing the DFT-based band structure using MLWFs.[66,67] Convergence is achieved by choosing a coarse 24 × 24 × 1 electronic grid for self-consistent calculations and a very dense 220 × 220 × 1 electronic grid for the subsequent thermoelectric calculations.

2.3 Classical molecular dynamics simulations

For the analysis of the C_{16} mechanical properties, we adopted an advanced approach based on machine learning interatomic potentials (MLIP).[68] These potentials have been proven highly effective in overcoming the limitations of more standard methods, such as empirical interatomic potentials (EIP).[69] MLIPs enable the integration of *ab initio* methods with classical molecular dynamics (MD) simulations, allowing for a detailed investigation of mechanical responses and fracture mechanisms in diverse materials, using interatomic potentials explicitly obtained for the investigated systems.

Here, we developed a specific force field for C_{16} based on the moment tensor potential (MTP),[70] trained with data generated from AIMD simulations in VASP. These molecular dynamics simulations were performed on supercells containing 64 atoms, covering uniaxial and biaxial strain changes to reduce the high correlation among the training data. Additionally, dynamics with progressive heating (heat ramps) were considered, resulting in 6500 training data points. This approach has been extensively validated in the literature, demonstrating success in predicting the mechanical properties of several nanomaterials.[42,71,72]

For MD simulations using the trained MLIP, we employed the LAMMPS software (large-scale atomic/molecular massively parallel simulator).[73] We have used the Velocity-Verlet algorithm to integrate Newton's equations of motion,[74] with a time step of 0.05 fs. After optimizing the systems using the obtained MLIP, we carried out two additional steps on the structures for the tensile loading simulations. The release of any residual stresses was controlled through simulations in an isobaric-isothermal (NPT) ensemble for 100 ps, using a Nosé–Hoover thermostat[75] to ensure thermal equilibrium and control. The temperature was set to 300 K and the external pressure to zero. For further tests and/or comparisons, an additional simulation run of 100 ps was performed using a canonical ensemble (NVT) at ambient temperature.

To evaluate the accuracy of the trained MLIP, we compared the phonon dispersion curves obtained using the MLIP with those calculated from density functional perturbation theory (DFPT). The phonon spectra showed excellent agreement (as shown Fig. 2), particularly in the acoustic modes, which are crucial for predicting thermal and mechanical properties. This validation step confirmed that the MLIP could reliably reproduce the harmonic vibrational properties of the system.

The elastic properties and fracture patterns were evaluated at 300 K, applying a uniaxial strain rate of 10^{-6} fs^{-1} along the x and y directions separately. The system was considered periodic in all directions, with pressure adjustments made perpendicular to the direction of the strain. The stress was calculated using the stress tensor for each atom, taking into account the virial contributions and atomic mass. Since the system is two-dimensional, the volume was defined based on the dimensions L_x and L_y, adopting a thickness of 3.35 Å, consistent with the literature.[76]

3 Results

This section examines the physicochemical properties of C_{16} based on the simulations using the abovementioned methodologies. We have explored its structural characteristics, including energy stability, dynamics, and thermal properties. Additionally, we investigated its electronic, excitonic, optical, thermoelectric, and mechanical properties. Potential applications of C_{16}, such as in solar cells, are also discussed.

3.1 Structural stability

After the DFT geometry optimization, we observed that C_{16} remains in a fully planar conformation (purely sp^2 hybridization). The symmetric triangular rings have one bond length of 1.44 Å, shared with the 10-membered ring. The other two equal sides of the triangular rings have bond lengths of 1.38 Å, shared with the 8-membered rings. The corresponding bond angle values are 58.43° and 63.14°, respectively.

The 4-membered ring is a rectangle with one side with a bond length of 1.41 Å (shared with the hexagonal rings) and the other with 1.54 Å (shared with the octagonal rings). The bond angle values of the benzene rings vary from 117.5° to 120.8°117.5. For the octagonal rings, the bond angle values range from 115.4° to 148.4°, while for the decagon ring, the values vary from 118.4° to 173.7°. The C_{16} lattice vectors are 6.48 Å and 7.15 Å for the horizontal and vertical directions, respectively. C_{16} belongs to the *Pmmm* ($D_{2h}{}^{1}$) symmetry group.

To determine the C_{16} stability, we have calculated the cohesive energy value, $E_{coh/atom} = (E_{tot} - 16{\cdot}E_C)/16 = -7.1$ eV per atom. The dynamical structural stability was verified by calculating the phonon dispersion band structure using density functional perturbation theory (DFPT) and MTP. The results are consistent and presented in Fig. 2. There is a close similarity in the acoustic modes. The differences in the optical modes are more pronounced. These results validate the trained MLIP. Additionally, the absence of imaginary frequencies suggests that C_{16} is structurally stable. There are two flat modes, around 54 THz and 59 THz. The lack of vibrational modes with frequencies exceeding 60 THz is consistent with the sp^2 hybridization since very high vibrations are typically associated with an sp hybridization.

To further assess the system's stability, Fig. 3 presents the temporal evolution of the total energy of a C_{16} supercell with an approximate area of 100 × 100 $Å^2$, obtained from a classical molecular dynamics (MD) simulation. This simulation employed an MLIP, whose details will be discussed later, and was conducted at a temperature of 300 K over a simulation time of 50 ps. The results indicate that the system's total energy is conserved, as expected. The inset of the figure shows front and side views of the C_{16} structure, revealing no signs of

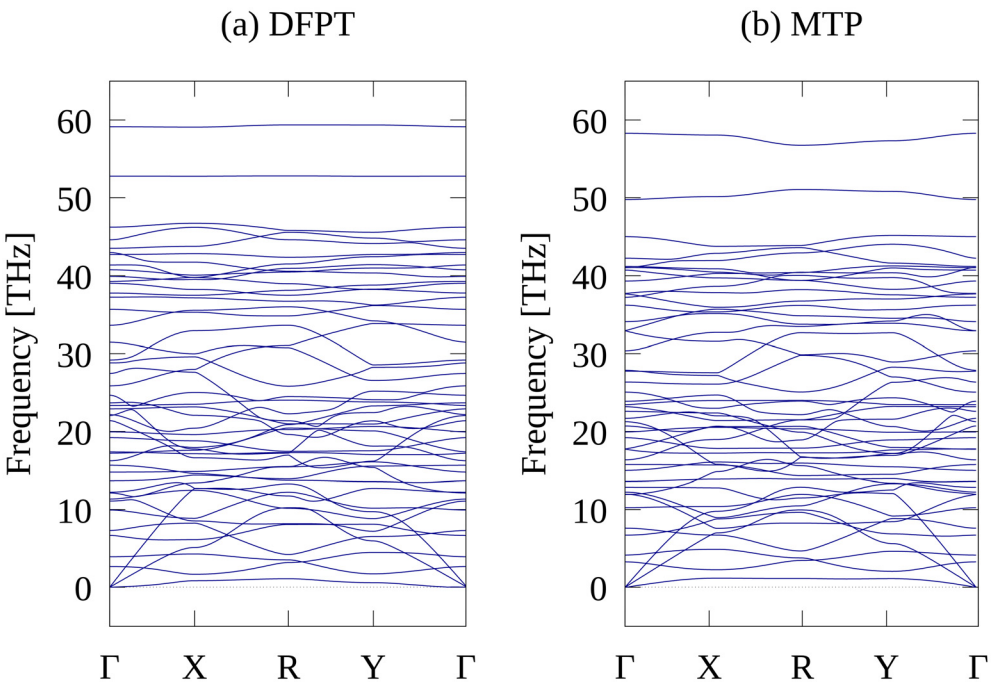

Fig. 2 Phonon dispersion spectrum of the C_{16} monolayer obtained using (a) DFTP and (b) MTP.

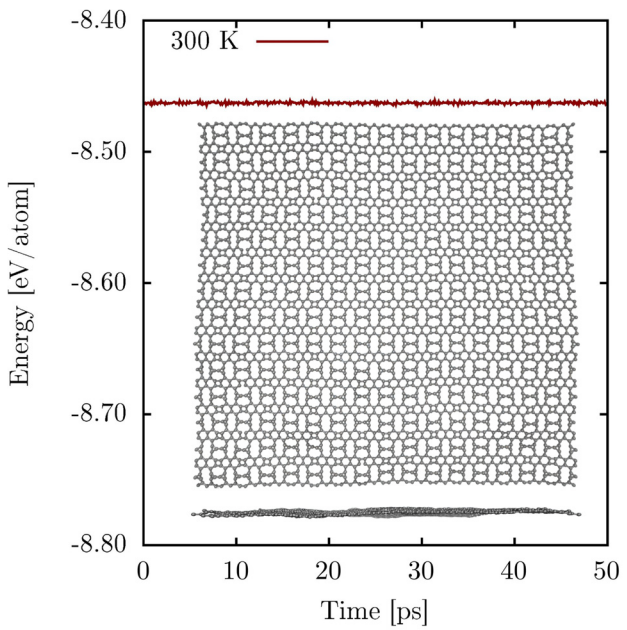

Fig. 3 C_{16} total energy values per atom as a function of the AIMD simulation. The insets show the top and lateral views of the final snapshot.

atomic reconfiguration, bond rearrangement, or bond breaking. Furthermore, the side view displays no significant fluctuations beyond those expected from thermal motion.

Additionally, to further confirm the mechanical stability of the C_{16} monolayer, we computed its in-plane elastic constants using the stress–strain method within the DFT framework. For a two-dimensional rectangular lattice, mechanical stability is ensured if the Born–Huang criteria are satisfied: $C_{11} > 0$, $C_{22} > 0$, $C_{66} > 0$, and $C_{11}C_{22}–C_{12}^2 > 0$. In the case of the nanomaterial investigated here, all these criteria are met, confirming the mechanical stability of the C_{16} monolayer. A detailed discussion of the mechanical properties of the system, including its fracture behavior, is provided in a subsequent section.

To assess the feasibility of isolating the C_{16} monolayer from a hypothetical bulk-like structure, we estimated its exfoliation energy by considering the energy difference between the isolated monolayer and a weakly stacked multilayer configuration. Due to its highly porous topology, the interlayer van der Waals interactions in C_{16} are expected to be significantly weaker than those in non-porous carbon allotropes. Based on comparisons with experimentally realized porous systems such as graphdiyne and biphenylene networks, we obtained the exfoliation energy of C_{16} to be approximately 13 meV $Å^{-2}$. This value is substantially lower than the exfoliation energy of graphene, which is approximately 20–25 meV $Å^{-2}$,[77] indicating that mechanical or liquid-phase exfoliation of C_{16} should be energetically favorable.

Although the present study focuses on the monolayer properties of C_{16}, it is crucial to consider the possible structural consequences if multiple layers were to be stacked. The undulations observed in the AIMD simulations (Fig. 3) are characteristic of low-energy out-of-plane fluctuations at finite temperature and do not compromise the monolayer's planarity under equilibrium. However, in a multilayer configuration, the weak van der Waals interactions expected due to the porous topology and relatively low charge density in the out-of-plane direction could result in poor interlayer registry. As a consequence, C_{16} may naturally adopt a turbostratic stacking

arrangement, similar to what has been experimentally observed in multilayer graphene systems. In such cases, rotational and translational misalignment between layers can occur, leading to a disordered stacking with minimal impact on in-plane symmetry. This behavior, often observed in porous or low-density 2D carbon frameworks, preserves the monolayer's electronic and mechanical characteristics while reducing interlayer coupling effects.

3.2 Electronic, excitonic, and optical properties

The electronic band structure and the corresponding projected density of states (PDOS) are presented in Fig. 4(a) and (b), respectively. Our system has a direct HSE06 (PBE) band gap of 0.59 eV (0.36 eV) localized near the Y high-symmetry point along the Y–Γ path. From the PDOS, we can observe that the main orbital contributions around the Fermi level come from the C p-orbitals, complemented by a minimal contribution of the C s-orbitals within the region close to the valence band maximum (VBM).

The optical activity, derived from the sum of the overall optical transitions by considering the two highest valence bands and the three lowest conduction bands, was analyzed for linear and circularly polarized light at the IPA level. This information is illustrated in Fig. 5(a)–(d). For linear polarized light along the $\hat{x}$ direction (Fig. 5(a)) we have some optical activity in the entire Brillouin zone (BZ), with higher values at the BZ edges at $k_x = 0$ Å^{-1} and $k_y = \pm 0.4$ Å^{-1}, respectively, with a maximum oscillator force of 6 Å^2. When comparing the optical activity for the $\hat{y}$ polarization, shown in Fig. 5(b), the maximum values are in the same region of the previous panel; however, the oscillator force values are 10 times higher (~70 Å^2), with the optical activity concentrated at the BZ edges. These results show a large optical anisotropy, with the optical response much more intense along the $\hat{y}$ direction.

Fig. 5(c) and (d) illustrate the optical activity for circular light polarization, obtained from a linear combination of $\hat{x}$ and $\hat{y}$ linear polarizations. The isotropic behavior observed in this case results from the dominant optical activity for the $\hat{y}$ polarization, as the $\hat{x}$ contribution is significantly smaller, resulting in a practically identical linear optical response under optical helicity.

The lowest energy excitonic levels, for direct (at Γ) and indirect (any other k-points) excitons, are shown in Fig. 6, the x-axis representing the excitonic momentum along the k-path, passing through the high symmetry points in the BZ. The excitonic ground state is direct, evidenced by the direct band gap observed in the electronic band structure. When compared with the fundamental electronic band gap, it results in an exciton binding energy of 96 meV, which is higher if compared to bulk values but lies within the lower limit for 2D carbon allotropes, where the expected exciton binding energy resides in the range [80 meV to 500 meV].[34]

The linear optical response, at the IPA and BSE levels considering linear and circular light polarizations, through the evaluation of the absorption coefficient, refractive index, and

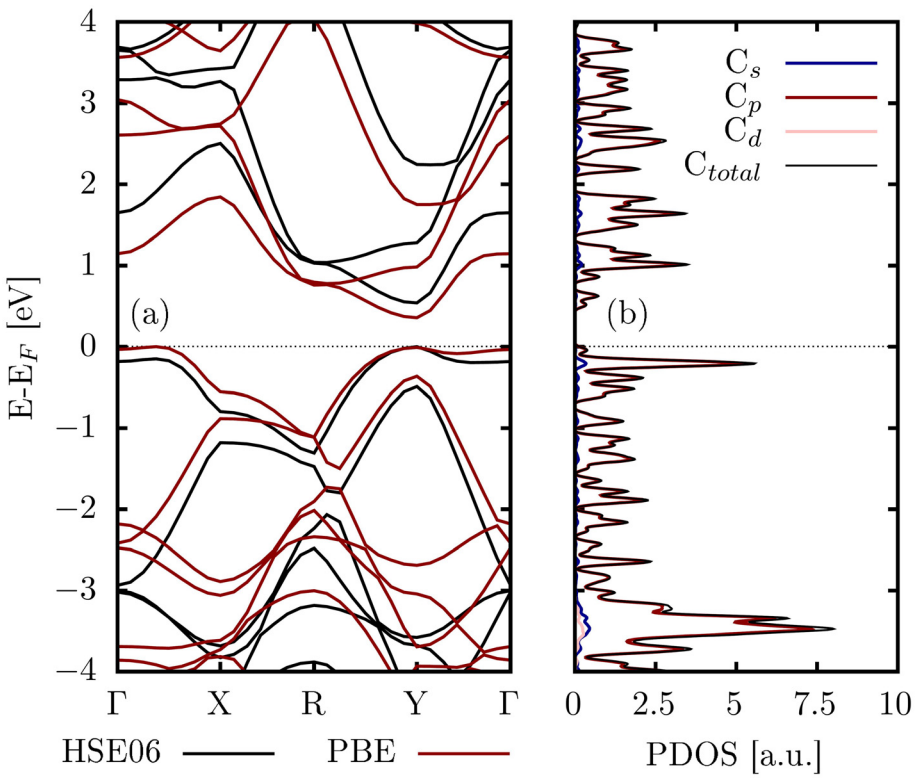

Fig. 4 (a) C_{16} electronic band structure at the PBE (red curves) and HSE06 (black curves) levels and (b) the HSE06 projected density of states on the s-, p-, and d-orbitals. The Fermi level is set at 0 eV.

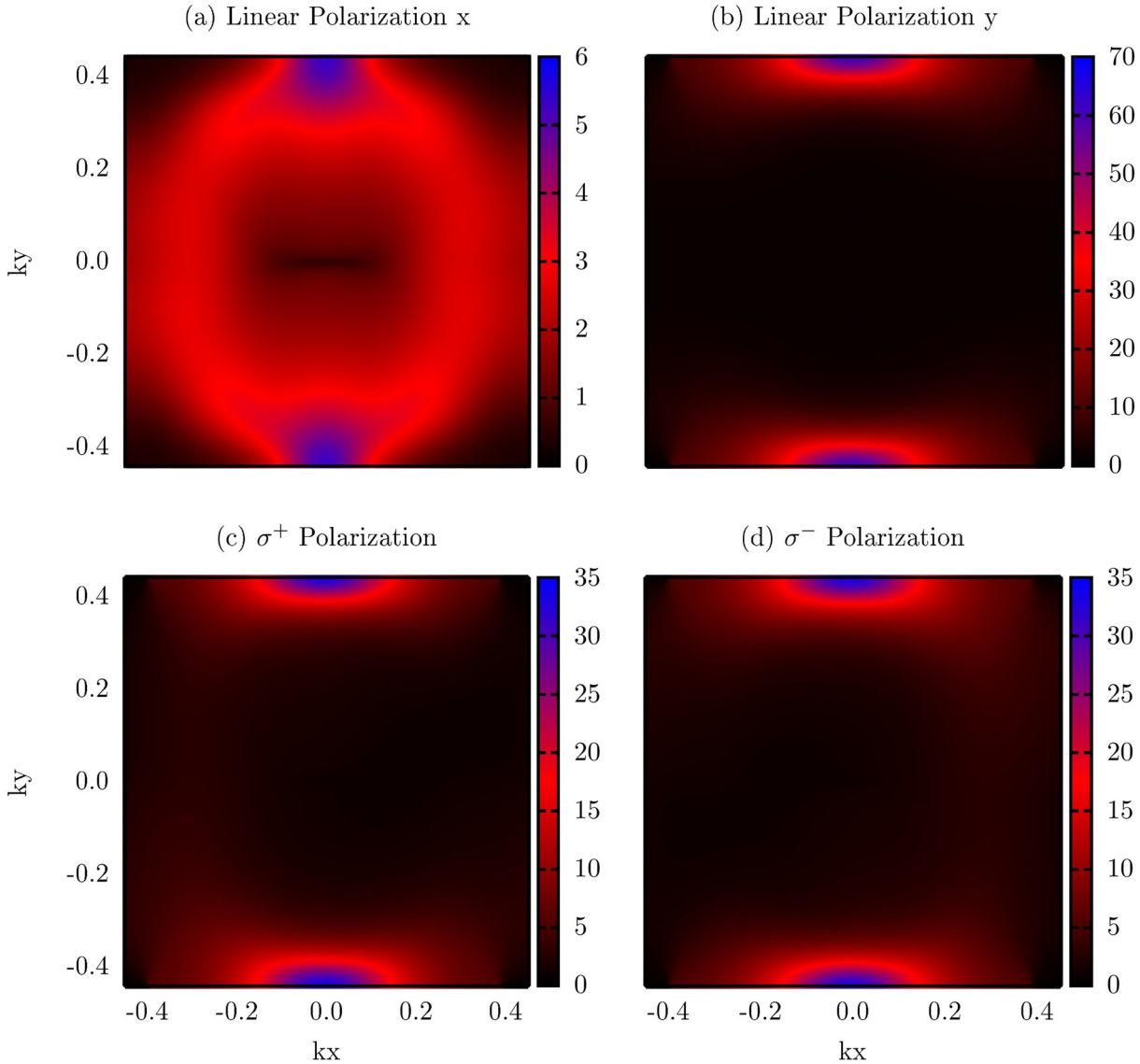

Fig. 5 Optical activity of the C_{16} monolayer in the first Brillouin zone for different light polarizations. (a) and (b) show oscillator strength maps (in Å^2) for linearly polarized light along the *x* and *y* directions, respectively. (c) and (d) correspond to circular polarizations: σ^+ (clockwise) and σ^- (counterclockwise). The color scale represents the intensity of optical transitions in reciprocal space through oscillator strength values (in Å^2), revealing pronounced anisotropy, particularly enhanced optical activity along the *y* direction.

reflectivity, is shown in Fig. 7(a)–(f). Fig. 7(a) and (d) demonstrate that C_{16} excitonic band structure obtained using an HSE06 parametrization in an MLWF-TB model absorbs in the infrared, visible, and ultraviolet regions. The excitonic effects result in a slight red shift in the absorption peaks. We also observe a substantial change in the linear optical response, giving rise to an essential optical anisotropy for linear light polarization because the absorption coefficient is much more intense for light polarization along the $\hat{y}$ direction. This result is consistent with the optical activity shown in Fig. 5. In contrast, for light excitations above 3.0 eV, the absorption coefficient is much more intense for $\hat{x}$ light polarization. The optical response is isotropic for circularly polarized light for the reasons mentioned above.

The optical anisotropy, under linear light polarization and the isotropic behavior for the circular one, is also seen in the refractive index (Fig. 7(b) and (e)) and the reflectivity (Fig. 7(c) and (f)). Under linear light polarization, the refractive index is higher for the $\hat{y}$ polarization in the infrared and visible spectrum regions. In the ultraviolet region, it is more pronounced for the $\hat{x}$ polarization. This index varies in the range of 0.9 to 2.4 and 1.28 to 2.4 for the $\hat{y}$ and $\hat{x}$ polarizations, respectively. This range is slightly narrowed when excitonic effects are considered (BSE level).

This behavior is similar to reflectivity that lies in the range of 0% to 20% for the $\hat{y}$ polarization case and 3% to 5% for the $\hat{x}$ polarization case. It is also interesting to observe that none of the incident photons are reflected for $\hat{y}$ polarization in the ultraviolet region. When circular light polarizations are con-

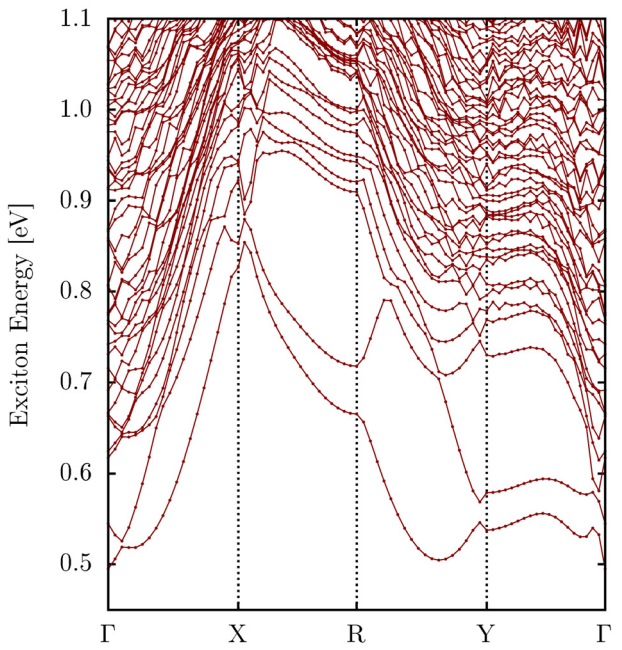

Fig. 6 Excitonic band structure of C_{16} calculated using the MLWF-TB model with HSE06 parametrization. The horizontal axis follows the high-symmetry path in the Brillouin zone, while the vertical axis represents the exciton energies (in eV). The lowest energy exciton is direct, *i.e.* electron and hole pairs located at the same *k*-point, which results in its localization at Γ point, with an estimated binding energy of approximately 96 meV.

sidered, both refractive index and reflectivity are the same, independent of clockwise (σ_-) or counterclockwise (σ_+) light polarization.

We can estimate the C_{16} solar harvesting efficiency through the electronic and optical properties data, using the power conversion efficiency (PCE) as a descriptor. The PCE was obtained by two methods: the Shockley–Queisser limit (SQ)[78] and the spectroscopy-limited maximum efficiency (SLME).[79] The former is directly obtained by the fundamental electronic band gap E_g when excitonic effects are not considered or through the exciton ground state energy Ex_{gs}; this kind of approach considers that all photons with energies equal or higher than E_g or Ex_{gs} are absorbed. The latter approach, which goes beyond E_g and Ex_{gs}, also considers the optical band gap or the exciton bright ground state energy when the excitonic effects are taken into account. Here, the absorption spectrum and the material thickness are the two fundamental parameters required to estimate the optical absorbance, which determines the rate of incident photon absorption. For 2D materials, the value of van der Waals length (3.21 Å) is added. This procedure is based on the work of Bernardi *et al.*,[80] where it was used to estimate graphene's absorbance due to its atomic thickness, yielding results consistent with experimental data. For both approaches, the PCE was also estimated considering the solar cell at 300 K and considering the AM1.5G model for the solar emission spectrum.[81] It is equally important to understand that both methods provide an upper limit of the solar harvesting efficiency and that experimentally reaching these values can demand years of research. Details of the theoretical formalism behind both methods can be found in previous works.[58,82]

The SQ-limit estimates a PCE^{SQ} of 17.06% when excitonic effects are not considered; yet, when quasiparticle effects are taken into account, the value is reduced to 12.96%, due to the exciton binding energy, which results in Ex_{gs}, being smaller than E_g. The SQ-limit curve has a maximum PCE^{SQ} when either E_g or Ex_{gs} comes closer to 1.31 eV; the further E_g or Ex_{gs} are from this ideal value, the lower is PCE^{SQ}. The SLME values (PCE^{SLME}) are significantly lower than those obtained through the previous approximation, resulting in a solar harvesting efficiency of less than 0.08%, regardless of whether quasi-particle effects are present. This low efficiency is primarily due to the material's monolayer thickness, which results in a poor photon absorption rate, as most incident photons pass through the material without being absorbed. Consequently, the material is almost transparent, presenting a considerable challenge for the use of 2D monolayers in photovoltaic devices.

Based on the investigation of Jariwala and co-workers,[83] which proposes a solution for this problem using light trapping techniques to enhance the absorbance rate closer to 100% in 2D materials, we made another estimation of PCE ($PCE_{max}{}^{SLME}$), adapting the SLME method, and considering the absorbance rate as a Heaviside function, where we adopt the value of 1 for incident photons with energy equals or higher than the optical band gap or exciton bright ground state and 0 otherwise. $PCE_{max}{}^{SLME}$ evaluates to an efficiency of 12.96% with excitonic effects considered and 17.05% when they are absent, suggesting a potential application of this monolayer as a solar harvesting absolver if light trapping schemes are applied.

The above results are consistent with previous investigations of 2D carbon allotropes for photovoltaic applications.[34] It is crucial to report the performance characteristics (PCE) both with and without excitonic effects, as the exciton binding energy is highly sensitive to the surrounding dielectric environment. Excitonic effects tend to be reduced by proximity interactions when a monolayer is in contact with other materials. This scenario is particularly relevant in solar cells, where the absorber layer is sandwiched between the electron and hole transport layers, leading to experimentally lower excitonic effects. In this work, we have explored both extremes: the excitonic maximum impact, which occurs when the monolayer is in a vacuum, and the complete absence of these quasi-particle effects, which provides a more realistic value for the PCE. The actual performance is expected to fall somewhere between these two extremes.

3.3 Thermoelectric properties

The effectiveness of a material in thermoelectric devices is measured by probing its figure of merit (zT)[84,85] defined as:

$$zT = \frac{S^2\sigma}{\kappa_e + \kappa_L},$$

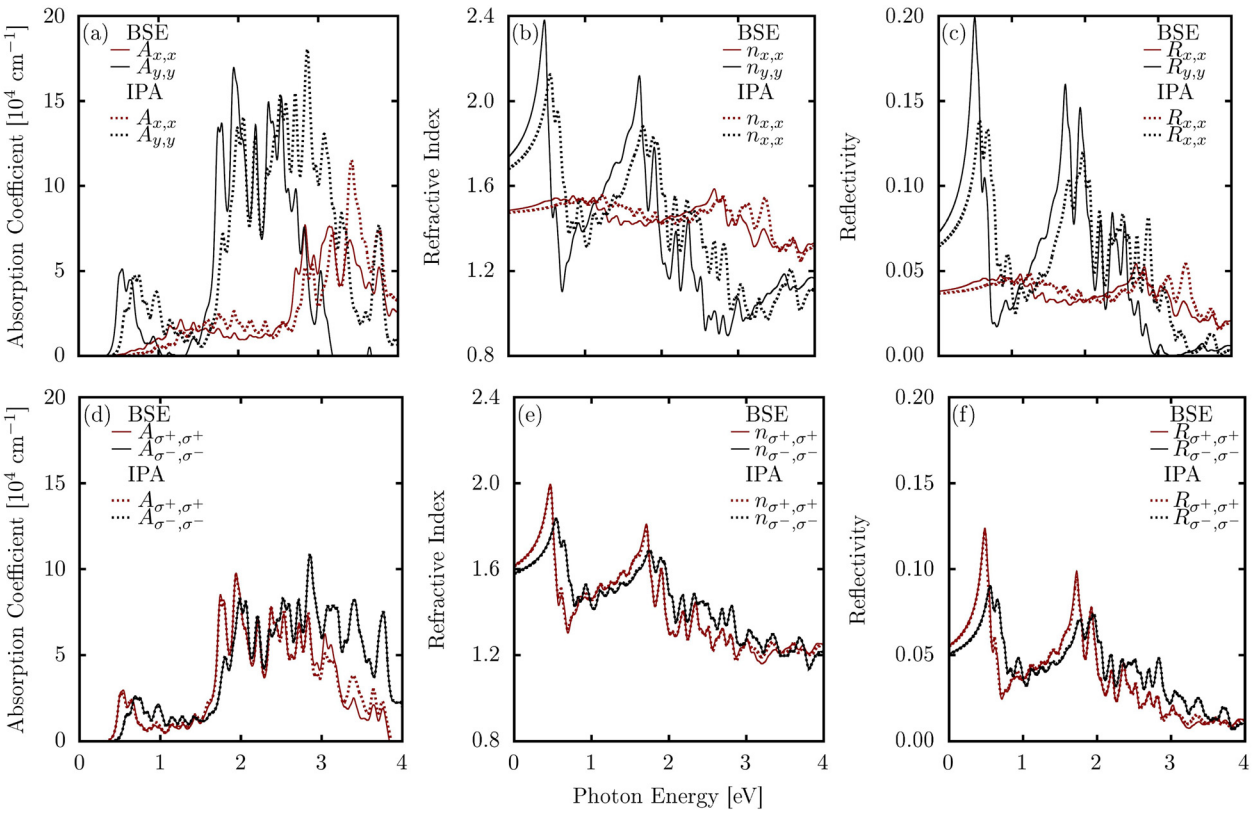

Fig. 7 Linear optical response of the C_{16} monolayer calculated using the Bethe–Salpeter equation (BSE, solid lines) and the independent particle approximation (IPA, dashed lines). (a and d) Absorption coefficient (in cm^{-1}), (b and e) refractive index (dimensionless), and (c and f) reflectivity (in %) are shown for linear (a–c) and circular (d–f) light polarizations. The red and black curves denote the polarizations x and y for linear light, and σ^+ and σ^- for circular light, respectively. The data demonstrate significant anisotropy under linearly polarized light and isotropy under circularly polarized light.

where S is the Seebeck coefficient and σ the electronic conductivity; κ_e and κ_L are the thermal electronic and thermal lattice conductivities, respectively. The quantity $S^2\sigma$ is known as the power factor (PF), representing the ability to produce electrical power from temperature gradients. Within the Boltzmann transport theory,[86,87] the tensor components of these physical quantities, except κ_L, can be extracted by evaluating:

$$\kappa_e^{\alpha\beta}(E) = \sum_{n,k} \tau_{n,k} v_g^{\alpha}(n,k) v_g^{\beta}(n,k) \delta(E - E_{n,k})$$

$$\sigma^{\alpha\beta}(T,\eta) = \frac{e^2}{NV} \int \sum_{n,k} \tau_{n,k} v_g^{\alpha}(n,k) v_g^{\beta}(n,k) \times \delta(E - E_{n,k}) \left[-\frac{\partial f(T,E,\eta)}{\partial E} \right] \mathrm{d}E$$

$$S^{\alpha\beta}(T,\eta) = \frac{1}{eVT\sigma^{\alpha\beta}(T,\eta)} \int \kappa_e^{\alpha\beta}(E-\eta) \times \left[-\frac{\partial f(T,E,\eta)}{\partial E} \right] \mathrm{d}E.$$

e is the electron's charge, T is temperature, E represents energy, N is the number of electronic (k-points) sampled in the Brillouin zone, V is the volume of the unit cell, and η is the chemical potential. Moreover, f is the Fermi–Dirac distribution function, δ is the Dirac delta function, $E_{n,k}$ is the energy of the n^{th} band at the k^{th} wave vector, and $\tau_{n,k}$ is the electron/hole lifetime at point (n,k) in the E–k plane. Likewise, v_g^{α} is the α^{th} component of the group velocity v_g. It should be noted that S is independent of the electronic lifetime, whereas σ and κ_e are not.

The computation of $\tau_{n,k}$ requires the knowledge of the imaginary part of the electron's self-energy, deduced by evaluating electron–phonon matrix elements on a highly dense electronic grid. Since this is a burdensome job and since one single value of τ per carrier charge is requisite for the BoltzWann code, the electronic lifetime will be directly obtained from the mobility values of the 2D C_{16} structure ($\mu_{2D,i}$) *via* the expression:

$$\tau_i = \frac{\mu_{2D,i} m_i^*}{e},$$

with i referring to electrons (e) or holes (h). Along the x and y directions, $\mu_e > \mu_h$ and $\tau_e > \tau_h$ at all temperatures.

On the other hand, κ_L is determined *via*:

$$\kappa_L^{\alpha\beta} = \frac{1}{NV} \sum_{\mathbf{q},s} c_v(\mathbf{q},s) v_g^{\alpha}(\mathbf{q},s) v_g^{\beta}(\mathbf{q},s) \tau(\mathbf{q},s),$$

where c_v is the phonon specific heat capacity and $\tau(\mathbf{q}, s)$ is the phonon lifetime of vibrational mode s at the $\mathbf{q}^{th}$ (phonon) point. This calculation can be performed using the PHONO3PY code,[88,89] which requires the tedious evaluation of third-order anharmonic constants. Such estimation is computationally very heavy, especially when the unit cell comprises many atoms.

As an alternative, and assuming that the acoustic phonons only participate in the heat transport in the structure, an empirical expression of κ_L, derived from the Slack model, could be employed:[90–93]

$$\kappa_L = A\frac{\bar{M}V^{1/3}{\theta_D}^3}{\gamma^2 nT}.$$

Here, $\bar{M}$ is the average atomic mass, n is the number of atoms in the unit cell, T is the temperature, and θ_D is the traditional definition of the Debye temperature.

γ is the Grüneisen parameter, which could be obtained from the PHONOPY code by running three phonon calculations, the first at the equilibrium volume and the others at slightly smaller and slightly larger volumes than the equilibrium one. Instead, it could be easily determined *via* an empirical expression that depends on the Poisson ratio (ν) of the material:[93,94]

$$\gamma = \frac{3}{2}\left(\frac{1+\nu}{2-3\nu}\right).$$

Since ν can be computed along any crystallographic direction, γ becomes direction-dependent too. On the other hand, A is a coefficient inherent in the Slack expression and dependent on γ such that:[93,95,96]

$$A = \frac{2.4\times10^{-6}}{1-\frac{0.514}{\gamma}+\frac{0.228}{\gamma^2}}.$$

It has been observed that this expression overestimates the values of κ_L in some materials.[97] However, this is currently our best approach until an experimental value of κ_L for the C_{16} monolayer becomes available. It should be noted that the Slack model is valid at temperatures larger than or equal to $\theta_{DA} = \theta_D/n^{1/3}$. In our case, θ_{DA} ~252.3 K, indicating that the model is credible for $T \geq 300$ K.

Fig. 8 illustrates C_{16} S, σ, κ_e, and PF along the x and y directions for T = 300 K, 600 K, and 1000 K. These quantities are plotted for chemical potential values 0.3 eV above and below the Fermi level to model electron and hole doping. For any temperature T, S is larger along the x direction. Except for S, the curves show some minor discontinuity when η approaches E_F from both sides due to the different electron and hole electronic lifetime values τ_e and τ_h (Table 1) as $\eta - E_F \to 0^+$ and $\eta - E_F \to 0^-$.

For the undoped C_{16}, that is for $\eta \sim E_F$ and T = 300 K, κ_e = 6.05 W (m K)$^{-1}$ along the x direction and κ_e = 22.79 W (m K)$^{-1}$ along the y-direction. These values increase as T increases, with the electronic thermal conductivity along the x direction always smaller than that along the y direction. More specifically, $\kappa_{e,xx}$ = 119.79 W (m K)$^{-1}$ and $\kappa_{e,yy}$ = 296.87 W (m K)$^{-1}$ at T = 600 K, and $\kappa_{e,xx}$ = 371.14 W (m K)$^{-1}$ and $\kappa_{e,yy}$ = 853.22 W (m K)$^{-1}$ at T = 1000 K.

Regarding the PF, we also observed that the values along the x direction are larger than those along the y one, at least for T = 300 and 600 K. At ambient temperatures, PF_{xx} = 9.70 mW (m K^2)$^{-1}$ while PF_{yy} = 3.36 mW (m K^2)$^{-1}$. At 600 K, PF_{xx} reaches a value of 0.11 W (m K^2)$^{-1}$ and PF_{yy} attains a value of 0.08 W (m K^2)$^{-1}$ (Fig. 9).

To eliminate the effect of vacuum in our flat structure, we will multiply κ_L by a factor of $S^{1/2}/V^{1/3}$, where 'S' denotes the area of the material at equilibrium. As can be seen from Fig. 10, the lattice thermal conductivity κ_L shows ultralow values along the x and y directions. At T = 300 K and for the undoped structure, $\kappa_{L,xx}$ = 1.9 × 10^{-2} W (m K)$^{-1}$ and $\kappa_{L,xx}$ = 1.87 × 10^{-2} W (m K)$^{-1}$. As T increases, κ_L lightly decreases so that $\kappa_{L,xx}$ = 0.99 × 10^{-2} W (m K)$^{-1}$, and $\kappa_{L,yy}$ = 0.93 × 10^{-2} W (m K)$^{-1}$ at 600 K. At 1000 K, $\kappa_{L,xx}$ = 0.59 × 10^{-2} W (m K)$^{-1}$, and $\kappa_{L,yy}$ = 0.56 × 10^{-2} W (m K)$^{-1}$.

To achieve a significant value of zT, a maximum value of PF, and a minimum value of the sum of the thermal conductivities are needed. As expected, the figure of merit along the x direction is higher. For the undoped structure, zT registers values of 0.06, 0.46, and 0.54 at T = 300 K, 600 K, and 1000 K, respectively.

Since the structure is thermally stable at 1000 K, a value of zT = 0.54 is relatively high; however, having zT values larger than or equal to 0.8 is desirable. Upon doping, zT_{xx} (zT_{yy}) reaches a maximum value of 0.94 (0.93) for energies 0.064 eV (0.093 eV) below E_F at ambient temperature. For T = 600 K, the maxima obtained values of 0.84 (0.77) for zT_{xx} (zT_{yy}) occurring at 0.086 eV (0.1 eV) below (above) E_F. At 1000 K, zT_{xx} has a maximum of 0.75 for an energy of 0.10 eV below E_F, while zT_{yy} depicts a maximum of 0.64 for an energy of 0.13 eV above E_F.

Knowing that energies below the Fermi level correspond to hole doping while those above to electron doping and that the farther we are from E_F, the heavier the doping, our best compromise is to induce a p-doping process capable of securing a zT_{xx} of 0.94 at T = 300 K, by just lowering E_F by just 0.064 eV. Considering that E_F is proportional to the hole density (n), then we can assume that $\Delta E_F/E_{F0} = \Delta n/n_0$, where E_{F0} and n_0 are the Fermi energy and electron/hole concentration for the undoped system, respectively; $\Delta E_F = E_F - E_{F0}$ and $\Delta n = n - n_0$, E_F being the Fermi energy and n the hole concentration of the doped system. We show that n/n_0 = 1.022, implying that n = $1.022n_0$, or $n \sim n_0$. Thus, by just lightly doping C_{16} with holes corresponding to a −0.064 eV shift in the Fermi energy, we can reach a zT as high as 0.94 along the x direction.

It is worth mentioning that the thermoelectric properties presented in this work were calculated within the constant relaxation time approximation (CRTA), where a representative electronic relaxation time τ was estimated from carrier mobility values. While this method is commonly employed in early-stage screening of thermoelectric materials due to its computational efficiency, it does not explicitly account for temperature- and energy-dependent electron scattering mechanisms,

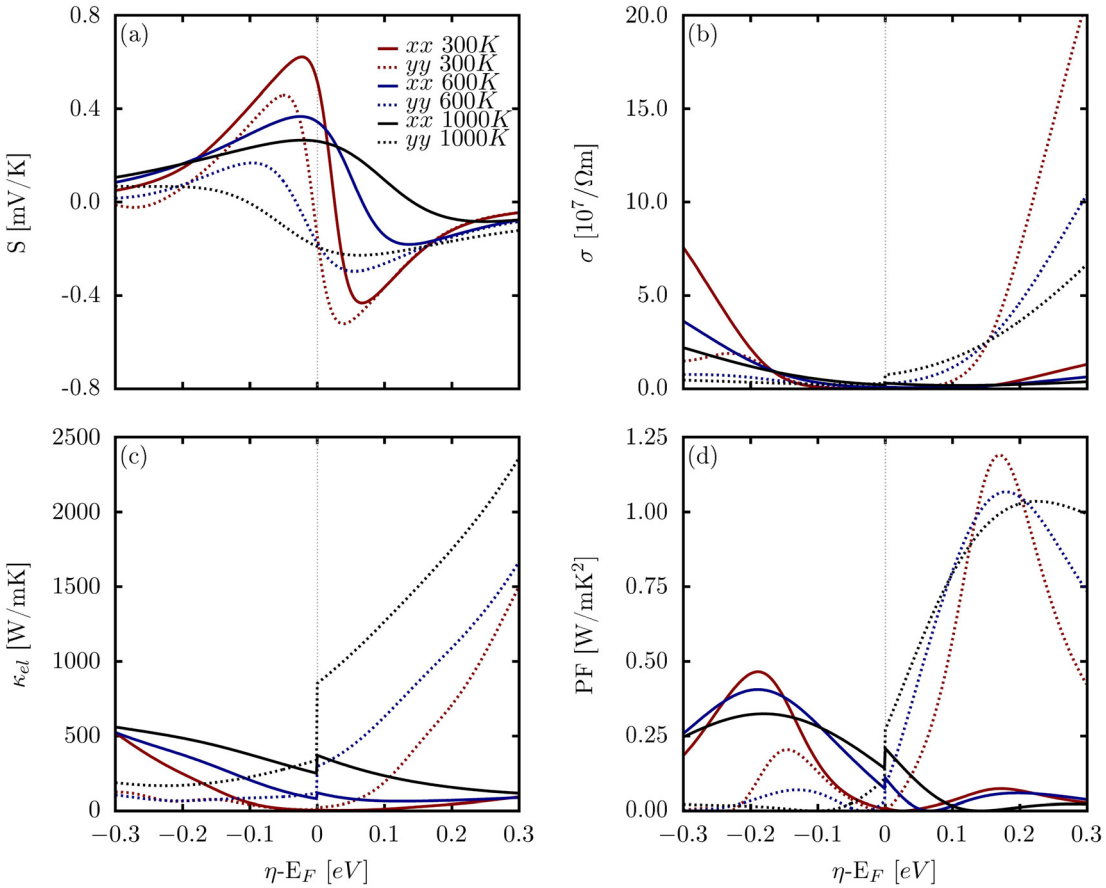

Fig. 8 (a) The change of the Seebeck coefficient, (b) the electronic conductivity, (c) the thermal electronic conductivity, and (d) the power factor as a function of electron and hole doping along the *x* and *y* directions at 300 K (red), 600 K (blue), and 1000 K (black).

Table 1 Calculated effective mass m_i^*, average effective mass m_d, in-plane stiffness C_{2D}, DP constant E_1, the charge carrier mobility μ, and the electronic lifetime τ at T = 300 K, 600 K, and 1000 K for the C_{16}. Here, m_0 is the mass of a free electron

Direction	Carrier	m_i^* (m_0)	m_d (m_0)	C_{2D} (eV Å^{-1})	E_1 (eV)	μ (10^3 cm^2 V^{-1} s^{-1})	τ (ps)
***T* = 300 K**							
x	e	0.15	0.021	6.19	−9.95	61.2	5.227
	h	0.29	0.081	6.19	−8.68	21.2	3.500
y	e	0.14	0.021	7.95	6.80	180.4	14.380
	h	0.28	0.081	7.95	7.68	36.01	5.739
***T* = 600 K**							
x	e	0.15	0.021	6.19	−9.95	30.6	2.613
	y	0.29	0.081	6.19	−8.68	10.5	1.734
y	e	0.14	0.021	7.95	6.80	90.2	7.190
	h	0.28	0.081	7.95	7.68	18.0	2.869
***T* = 1000 K**							
x	e	0.15	0.021	6.19	−9.95	18.4	1.571
	y	0.29	0.081	6.19	−8.68	6.4	1.05
y	e	0.14	0.021	7.95	6.80	54.1	4.312
	h	0.28	0.081	7.95	7.68	10.8	1.722

such as electron–phonon interactions, impurity scattering, or grain boundary effects. Consequently, the computed figure of merit (zT) values should be interpreted as upper limits. More rigorous approaches, such as those incorporating first-principles electron–phonon coupling or full Boltzmann transport calculations with explicit scattering rates, have been shown to provide more accurate predictions of transport coefficients.[98–100] Future work could adopt these advanced methods to refine the thermoelectric performance assessment of C_{16}.

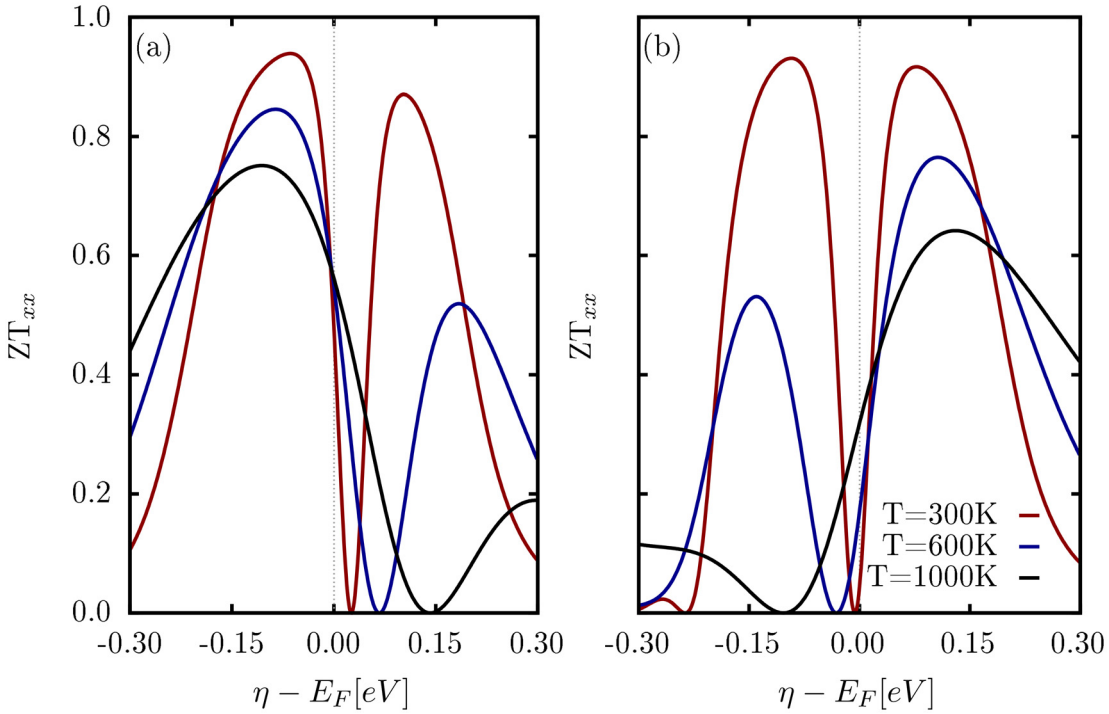

Fig. 9 Same as in Fig. 8 but for the figure of merit (zT) at 300 K, 600 K, and 1000 K along the (a) x and (b) y directions.

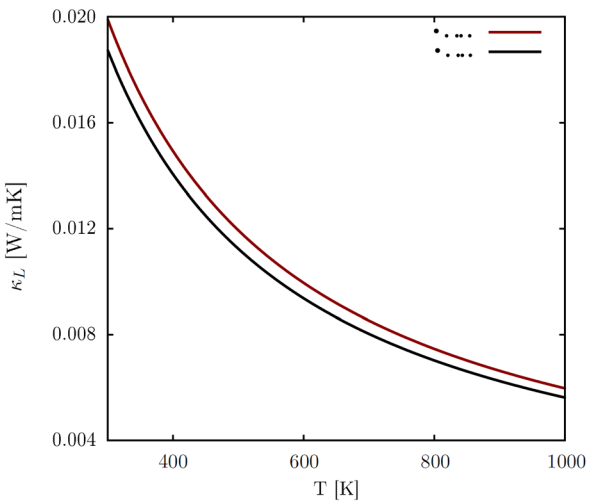

Fig. 10 Lattice thermal conductivity for $T \geq 300$ K, along the x- (red) and y-directions (black).

3.4 Mechanical properties

To understand the C_{16} mechanical response, we initially performed *ab initio* molecular dynamics (AIMD) simulations under various fixed strain values and with constant temperature variations. Based on these data, a machine learning interatomic potential (MLIP) was trained, which was then used to obtain the mechanical response of the system. A C_{16} 16 × 14 × 1 supercell containing 3584 atoms was subjected to deformations along the x and y directions up to a maximum of 15% of the respective initial length values.

In Fig. 11, we present the stress–strain curves obtained from these simulations. The red points represent the calculated stress for each deformation percentage along the x direction. In contrast, the blue points show the corresponding results for uniaxial deformation applied along the y direction. The system exhibits partially similar behaviors concerning hardness for these directions. Along the x direction, Young's modulus is approximately 500 GPa, while along the y one, this

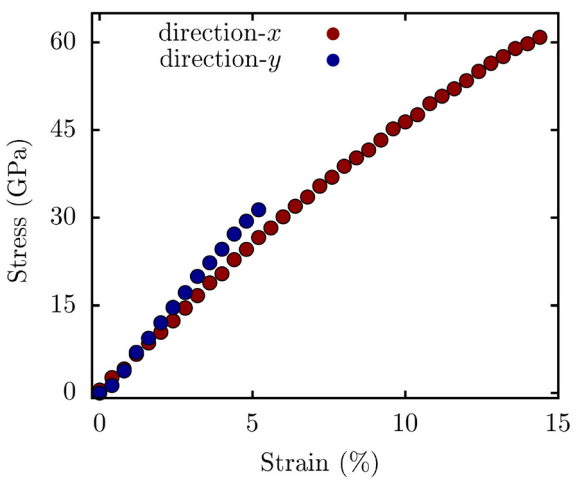

Fig. 11 Stress–strain curve, obtained using MLIP, for strain along the x- (red) and y-directions (blue).

value reaches nearly 630 GPa. Both cases display ductile characteristics; however, the stress accumulation along the *y* direction is higher, leading the structure to fracture at a strain of only 5.5%. On the other hand, along the *x* direction, the system endures nearly three times greater deformation, with a critical strain at 14.6%. Given these aspects, the maximum stress obtained for deformation along the *x* direction is approximately 61.7 GPa at 14.6% strain and 33.1 GPa along the *y* one at 5.5% strain.

To gain deeper insights into the C_{16} mechanical response, we present representative snapshots of C_{16} under several strain values in Fig. 12. Panels (a) and (d) depict the system's equilibrium state after residual stresses have been eliminated and the system thermalized at room temperature. The color gradient from blue to red represents the Von Mises (VM) stress,[101–104] which provides a better understanding of where the fractures originate and propagate.

In panel (b), the system is shown at a strain of 14.4% on the limit of fracturing. The strain is concentrated in the region, forming covalent chains of naphthalene, particularly in the rectangular rings, due to their limited flexibility in releasing the strain. Finally, panel (c) shows the system at a strain of 15%, where fracture occurs and a crack propagates, resulting in successive breakages of the hexagonal rings.

Along the *y* direction, panel (e) shows the system under 5% strain. Several bonds have reconfigured, and it is possible to observe that stress is concentrated mainly in the regions derived from the bicyclopropylidene molecule. This region proved to be more fragile due to the topology of the involved rings, which explains the early system failure under strain along this direction. After the atomic reconfiguration upon fracture (panel (c) – 5.6%), several bonds break, leading to the C_{16} complete structural failure.

Beyond identifying the location of fracture initiation, we investigated the underlying mechanism driving the mechanical failure of the C_{16} monolayer. As shown in the stress–strain analysis (Fig. 11) and the deformation snapshots (Fig. 12), fracture begins preferentially at the junctions between ring types, particularly in regions derived from the bicyclopropylidene motifs under *y*-direction strain, and in rectangular ring regions under *x*-direction strain. These regions contain bonds with distinct angles and local strain concentrations due to topological constraints.

To better understand the rupture behavior of the C_{16} monolayer, we analyzed the von Mises stress distribution during uniaxial tensile deformation, as shown in Fig. 12. This criterion enables the visualization of local mechanical stress concentrations across the structure. In the stress maps, blue regions indicate low stress levels, while red regions highlight areas of maximum stress concentration. Under strain along the *x* direction, fracture initiates near the rectangular rings, where the geometry imposes strong angular constraints and bond deformation. In contrast, under strain along the *y* direction, the stress is concentrated in regions derived from the bicyclopropylidene motifs, which exhibit higher curvature and lower structural symmetry.

As the strain increases, the red regions expand and coalesce, indicating the path of stress propagation leading to rupture. These high-stress zones precede the formation of cracks, confirming that mechanical failure is not random but follows predictable stress accumulation patterns. The von Mises stress analysis also aligns with the electronic charge dis-

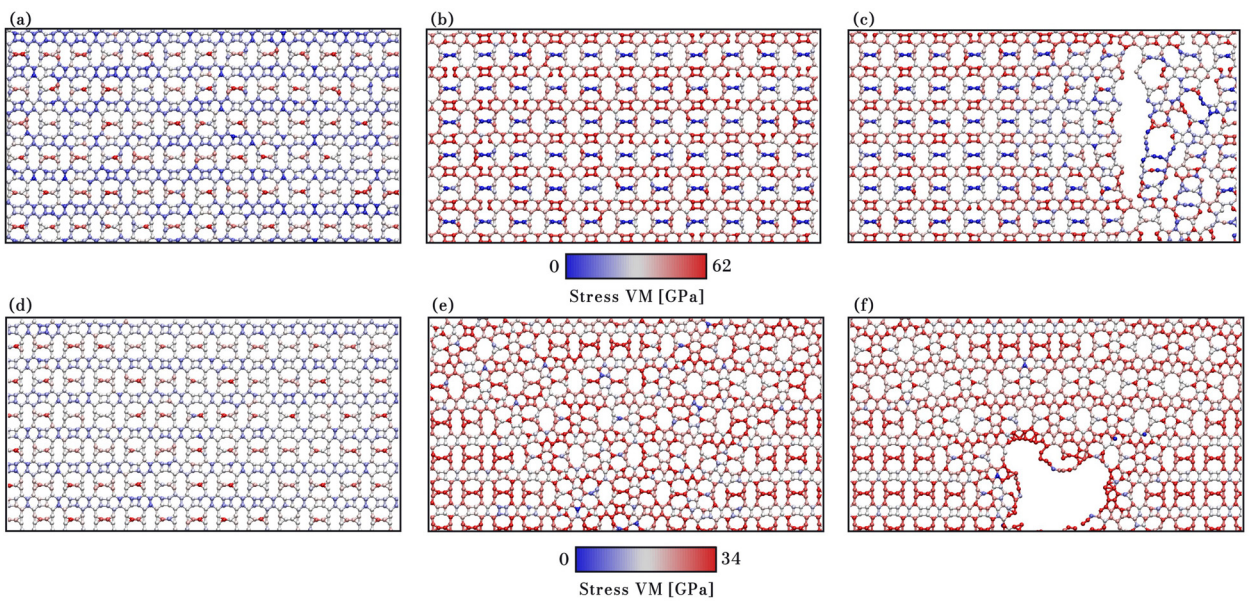

Fig. 12 Representative snapshots of the C_{16} monolayer at different stages of the deformation process along the *x* (a–c) and *y* (d–f) directions. The deformations shown are at (a) 0%, (b) 14.4%, and (c) 14.7% along the *x* direction, and (d) 0%, (e) 5.3%, and (f) 5.6% along the *y* one.

tribution shown in Fig. 1, where the initial rupture zones correspond to bonds with lower charge density, suggesting weaker delocalization. This combined structural and electronic interpretation highlights the relationship between topology, local bonding environment, and fracture mechanisms in porous 2D carbon allotropes, such as C_{16}.

4 Conclusions

In summary, we propose a novel two-dimensional carbon allotrope exhibiting semiconductor behavior. We performed first-principles simulations based on the density functional theory (DFT) formalism and atomistic simulations using a reactive force field trained through machine learning to characterize this novel nanomaterial. We conclude that the C_{16} monolayer demonstrates promising physical and chemical properties, particularly in applications involving electronic devices and energy conversion. Electronically, 2D-C_{16} displays a direct bandgap of 0.59 eV, making it suitable for optoelectronic device applications. Its optical properties demonstrate anisotropic absorption along the y direction, with the material having an exciton binding energy of 96 meV, confirming its potential in photovoltaic applications. The material exhibits a power conversion efficiency (PCE_{max}^{SLME}) of 13% when all photons are absorbed and excitonic effects are taken into account. The structure possesses ultralow planar lattice thermal conductivities of 1.9×10^{-2} W (m K)$^{-1}$ and 1.87×10^{-2} W (m K)$^{-1}$ along the x and y directions, respectively. The thermoelectric figure of merit (zT) can reach 0.93 at room temperature near the Fermi level, indicating that C_{16} can be utilized in thermoelectric devices. Additionally, the anisotropic mechanical strength of C_{16} is significant, with Young's moduli of 500 GPa for the x direction and 630 GPa for the y one, characterizing it as a ductile and robust material under mechanical stress.

Author contributions

K. A. L. L: data curation, simulation, software, investigation, writing – original draft. R. A. F. A.: data curation, simulation, investigation, visualization. E. A. M.: data curation, simulation, investigation, visualization, writing – original draft. A. C. D: data curation, software, simulation, investigation, writing – original draft. D. S. G.: investigation, writing – review, supervision, funding acquisition. M. L. P. J.: investigation, writing – original draft, funding acquisition. L. A. R. J.: conceptualization, investigation, writing – review, supervision, funding acquisition.

Data availability

The datasets supporting the findings of this study are available, including the optimized CIF structure of C_{16} and the force field parameters based on machine learning. The authors may provide additional data upon reasonable request.

Conflicts of interest

There are no conflicts to declare.

Acknowledgements

The authors are thankful for financial support from the National Council for Scientific and Technological Development (CNPq, grant numbers 408144/2022-0 and 305174/2023-1), Federal District Research Support Foundation (FAPDF, grant numbers 00193-00001817/2023-43 and 00193-00002073/2023-84), the Coordination for Improvement of Higher Level Education (CAPES). In addition, the authors thank the "Centro Nacional de Processamento de Alto Desempenho em São Paulo" (CENAPAD-SP, UNICAMP/FINEP – MCTI project) for resources for the 897 and 570 projects, Lobo Carneiro HPC (NACAD) at the Federal University of Rio de Janeiro (UFRJ) for the 133 project. L. A. R. J. acknowledges the financial support from FAPDF grant 0193.000942/2015, CNPq grant 350176/2022-1, and FAPDF-PRONEM grant 00193.00001247/2021-20. A. C. D. and L. A. R. J. also acknowledge PDPG-FAPDF-CAPES Centro-Oeste grant number 00193-00000867/2024-94. M. L. P. J. acknowledges financial support from FAPDF grant 00193-00001807/2023-16. Elie A. Moujaes thanks the financial support of the Brazilian National Council for Scientific and Technological Development, CNPq, grant number 315324/2023-6. K. A. L. L. and D. S. G. acknowledge the Center for Computing in Engineering and Sciences at Unicamp for financial support through the FAPESP/CEPID grant #2013/08293-7.

References

1 D. Suhag, P. Thakur and A. Thakur, *Integrated Nanomaterials and their Applications*, 2023, pp. 1–17.
2 A. Yadav, H. Kumar, R. Sharma and R. Kumari, *Surf. Interfaces*, 2023, **39**, 102925.
3 B. H. Alshammari, M. M. Lashin, M. A. Mahmood, F. S. Al-Mubaddel, N. Ilyas, N. Rahman, M. Sohail, A. Khan, S. S. Abdullaev and R. Khan, *RSC Adv.*, 2023, **13**, 13735–13785.
4 A. Lipovka, A. Garcia, E. Abyzova, M. Fatkullin, Z. Song, Y. Li, R. Wang, R. D. Rodriguez and E. Sheremet, *Adv. Opt. Mater.*, 2024, **12**, 2303194.
5 H. Yu, J. Zhang, I. Shaheen, M. Ahmad, X. Chen, B. Akkinepally and I. Hussain, *J. Ind. Eng. Chem.*, 2024, **129**, 53–68.
6 K. S. Novoselov, A. K. Geim, S. V. Morozov, D.-e. Jiang, Y. Zhang, S. V. Dubonos, I. V. Grigorieva and A. A. Firsov, *Science*, 2004, **306**, 666–669.
7 C. e. e. Rao, A. e. Sood, K. e. Subrahmanyam and A. Govindaraj, *Angew. Chem., Int. Ed.*, 2009, **48**, 7752–7777.
8 C. Lee, X. Wei, J. W. Kysar and J. Hone, *Science*, 2008, **321**, 385–388.

9 Z.-S. Wu, W. Ren, L. Gao, J. Zhao, Z. Chen, B. Liu, D. Tang, B. Yu, C. Jiang and H.-M. Cheng, *ACS Nano*, 2009, **3**, 411–417.
10 F. Perreault, A. F. De Faria and M. Elimelech, *Chem. Soc. Rev.*, 2015, **44**, 5861–5896.
11 G. Peschel, *Carbon-carbon bonds: hybridization*, 2011, accessed: 2024-10-05, **https://www.physik.fu-berlin.de/einrichtungen/ag/ag-reich/lehre/Archiv/ss2011/docs/Gina_Peschel-Handout.pdf**.
12 S. K. Tiwari, V. Kumar, A. Huczko, R. Oraon, A. D. Adhikari and G. Nayak, *Crit. Rev. Solid State Mater. Sci.*, 2016, **41**, 257–317.
13 H. Chang and H. Wu, *Adv. Funct. Mater.*, 2013, **23**, 1984–1997.
14 B. H. Nguyen and V. H. Nguyen, *Adv. Nat. Sci.: Nanosci. Nanotechnol.*, 2016, **7**, 043001.
15 E. H. Falcao and F. Wudl, *J. Chem. Technol. Biotechnol.*, 2007, **82**, 524–531.
16 R.-S. Zhang and J.-W. Jiang, *Front. Phys.*, 2019, **14**, 1–17.
17 R. Longuinhos, E. A. Moujaes, S. S. Alexandre and R. Nunes, *Chem. Mater.*, 2014, **26**, 3701–3708.
18 W. H. Brandão, A. L. Aguiar, A. F. Fonseca, D. Galvão and J. De Sousa, *Mech. Mater.*, 2023, **176**, 104503.
19 R. M. Tromer, L. R. Júnior, D. S. Galvão, A. C. Dias and E. A. Moujaes, *Mater. Today Commun.*, 2024, **39**, 109310.
20 H. W. Kroto, J. R. Heath, S. C. O'Brien, R. F. Curl and R. E. Smalley, *Nature*, 1985, **318**, 162–163.
21 S. Iijima and T. Ichihashi, *Nature*, 1993, **363**, 603–605.
22 Q. Fan, L. Yan, M. W. Tripp, O. Krejčí, S. Dimosthenous, S. R. Kachel, M. Chen, A. S. Foster, U. Koert, P. Liljeroth, *et al.*, *Science*, 2021, **372**, 852–856.
23 X. Liu, S. M. Cho, S. Lin, Z. Chen, W. Choi, Y.-M. Kim, E. Yun, E. H. Baek, H. Lee, *et al.*, *Matter*, 2022, **5**, 2306–2318.
24 Q. Li, Y. Li, Y. Chen, L. Wu, C. Yang and X. Cui, *Carbon*, 2018, **136**, 248–254.
25 V. G. Desyatkin, W. B. Martin, A. E. Aliev, N. E. Chapman, A. F. Fonseca, D. S. Galvão, E. R. Miller, K. H. Stone, Z. Wang, D. Zakhidov, *et al.*, *J. Am. Chem. Soc.*, 2022, **144**, 17999–18008.
26 S. He, B. Wu, Z. Xia, P. Guo, Y. Li and S. Song, *Nanoscale Adv.*, 2023, **5**, 2487–2492.
27 L. Hou, X. Cui, B. Guan, S. Wang, R. Li, Y. Liu, D. Zhu and J. Zheng, *Nature*, 2022, **606**, 507–510.
28 R. Baughman, H. Eckhardt and M. Kertesz, *J. Chem. Phys.*, 1987, **87**, 6687–6699.
29 A. Balaban, C. C. Rentia and E. Ciupitu, *Rev. Roum. Chim.*, 1968, **13**, 231–247.
30 S. Berber, E. Osawa and D. Tománek, *Phys. Rev. B: Condens. Matter Mater. Phys.*, 2004, **70**, 085417.
31 M. A. Hudspeth, B. W. Whitman, V. Barone and J. E. Peralta, *ACS Nano*, 2010, **4**, 4565–4570.
32 Z. Wang, X.-F. Zhou, X. Zhang, Q. Zhu, H. Dong, M. Zhao and A. R. Oganov, *Nano Lett.*, 2015, **15**, 6182–6186.
33 D. Malko, C. Neiss, F. Vines and A. Görling, *Phys. Rev. Lett.*, 2012, **108**, 086804.
34 A. Cavalheiro Dias, C. D. Almeida Cornélio, M. J. Piotrowski, L. A. Ribeiro Júnior, C. M. de Oliveira Bastos, C. R. Caldeira Rêgo and D. Guedes-Sobrinho, *ACS Appl. Energy Mater.*, 2024, **7**, 8572–8582.
35 H. Tang, C. M. Hessel, J. Wang, N. Yang, R. Yu, H. Zhao and D. Wang, *Chem. Soc. Rev.*, 2014, **43**, 4281–4299.
36 J. Li and Y. Han, *Giant*, 2023, **13**, 100140.
37 X. Chen, A. Bouhon, L. Li, F. M. Peeters and B. Sanyal, *Carbon*, 2020, **170**, 477–486.
38 X. Li, Q. Wang and P. Jena, *J. Phys. Chem. Lett.*, 2017, **8**, 3234–3241.
39 Y. Shen, J. Yu, J. Liu, Y. Guo, Y. Qie and Q. Wang, *J. Phys. Chem. C*, 2019, **123**, 4567–4573.
40 D. J. P. Beserra, A. Saraiva-Souza, E. M. Diniz, M. Fadel, V. Meunier and E. C. Girão, *Phys. Rev. Mater.*, 2020, **4**, 084003.
41 X. Wang, L. Chen, Z. Yuan, J. Rong, J. Feng, I. Muzammil, X. Yu, Y. Zhang and Z. Zhan, *J. Mater. Chem. A*, 2019, **7**, 8967–8974.
42 K. A. Lima, R. A. Alves, D. A. da Silva, F. L. Mendonça, M. L. Pereira and L. A. Ribeiro, *Phys. Chem. Chem. Phys.*, 2025, **27**, 8684–8691.
43 C. Moreno, M. Vilas-Varela, B. Kretz, A. Garcia-Lekue, M. V. Costache, M. Paradinas, M. Panighel, G. Ceballos, S. O. Valenzuela, D. Peña, *et al.*, *Science*, 2018, **360**, 199–203.
44 D. S. Parker, F. Zhang, Y. S. Kim, R. I. Kaiser, A. Landera, V. V. Kislov, A. M. Mebel and A. Tielens, *Proc. Natl. Acad. Sci. U. S. A.*, 2012, **109**, 53–58.
45 A. de Meijere, S. I. Kozhushkov and A. F. Khlebnikov, *Small Ring Compounds in Organic Synthesis VI*, 2000, pp. 89–147.
46 G. Kresse and J. Hafner, *Phys. Rev. B: Condens. Matter Mater. Phys.*, 1993, **48**, 13115–13118.
47 G. Kresse and J. Furthmüller, *Phys. Rev. B: Condens. Matter Mater. Phys.*, 1996, **54**, 11169–11186.
48 G. Kresse and D. Joubert, *Phys. Rev. B: Condens. Matter Mater. Phys.*, 1999, **59**, 1758–1775.
49 J. P. Perdew, K. Burke and M. Ernzerhof, *Phys. Rev. Lett.*, 1996, **77**, 3865.
50 A. J. Cohen, P. Mori-Sánchez and W. Yang, *Phys. Rev. B: Condens. Matter Mater. Phys.*, 2008, **77**, 115123.
51 J. M. Crowley, J. Tahir-Kheli and W. A. Goddard, *J. Phys. Chem. Lett.*, 2016, **7**, 1198–1203.
52 J. Heyd and G. E. Scuseria, *J. Chem. Phys.*, 2004, **121**, 1187–1192.
53 K. Hummer, J. Harl and G. Kresse, *Phys. Rev. B: Condens. Matter Mater. Phys.*, 2009, **80**, 115205.
54 H. J. Monkhorst and J. D. Pack, *Phys. Rev. B*, 1976, **13**, 5188–5192.
55 R. M. Martin, *Electronic structure: basic theory and practical methods*, Cambridge University Press, 2004.
56 S. Nosé, *J. Chem. Phys.*, 1984, **81**, 511–519.
57 A. A. Mostofi, J. R. Yates, Y.-S. Lee, I. Souza, D. Vanderbilt and N. Marzari, *Comput. Phys. Commun.*, 2008, **178**, 685–699.

58 A. C. Dias, J. F. Silveira and F. Qu, *Comput. Phys. Commun.*, 2023, **285**, 108636.
59 E. E. Salpeter and H. A. Bethe, *Phys. Rev.*, 1951, **84**, 1232–1242.
60 J. Deslippe, G. Samsonidze, D. A. Strubbe, M. Jain, M. L. Cohen and S. G. Louie, *Comput. Phys. Commun.*, 2012, **183**, 1269–1289.
61 D. Sangalli, A. Ferretti, H. Miranda, C. Attaccalite, I. Marri, E. Cannuccia, P. Melo, M. Marsili, F. Paleari, A. Marrazzo, G. Prandini, P. Bonfà, M. O. Atambo, F. Affinito, M. Palummo, A. Molina-Sánchez, C. Hogan, M. Grüning, D. Varsano and A. Marini, *J. Phys.: Condens. Matter*, 2019, **31**, 325902.
62 G. Pizzi, V. Vitale, R. Arita, S. Blügel, F. Freimuth, G. Géranton, M. Gibertini, D. Gresch, C. Johnson, T. Koretsune, *et al.*, *J. Phys.: Condens. Matter*, 2020, **32**, 165902.
63 A. A. Mostofi, J. R. Yates, G. Pizzi, Y.-S. Lee, I. Souza, D. Vanderbilt and N. Marzari, *Comput. Phys. Commun.*, 2014, **185**, 2309–2310.
64 C. A. Rozzi, D. Varsano, A. Marini, E. K. U. Gross and A. Rubio, *Phys. Rev. B: Condens. Matter Mater. Phys.*, 2006, **73**, 205119.
65 G. Pizzi, D. Volja, B. Kozinsky, M. Fornari and N. Marzari, *Comput. Phys. Commun.*, 2014, **185**, 422–429.
66 W. Kohn and J. R. Onffroy, *Phys. Rev. B*, 1973, **8**, 2485.
67 W. Kohn, *Phys. Rev.*, 1959, **115**, 809.
68 I. S. Novikov, K. Gubaev, E. V. Podryabinkin and A. V. Shapeev, *Mach. Learn.: Sci. Technol.*, 2020, **2**, 025002.
69 B. Mortazavi, I. S. Novikov, E. V. Podryabinkin, S. Roche, T. Rabczuk, A. V. Shapeev and X. Zhuang, *Appl. Mater. Today*, 2020, **20**, 100685.
70 A. V. Shapeev, *Multiscale Model. Simul.*, 2016, **14**, 1153–1173.
71 B. Mortazavi, M. Silani, E. V. Podryabinkin, T. Rabczuk, X. Zhuang and A. V. Shapeev, *Adv. Mater.*, 2021, **33**, 2102807.
72 B. Mortazavi, X. Zhuang, T. Rabczuk and A. V. Shapeev, *Mater. Horiz.*, 2023, **10**, 1956–1968.
73 S. Plimpton, *J. Comput. Phys.*, 1995, **117**, 1–19.
74 L. Verlet, *Phys. Rev.*, 1967, **159**, 98.
75 W. G. Hoover, *Phys. Rev. A*, 1985, **31**, 1695.
76 R. R. Nair, P. Blake, A. N. Grigorenko, K. S. Novoselov, T. J. Booth, T. Stauber, N. M. R. Peres and A. K. Geim, *Science*, 2008, **320**, 1308–1308.
77 R. Zacharia, H. Ulbricht and T. Hertel, *Phys. Rev. B: Condens. Matter Mater. Phys.*, 2004, **69**, 155406.
78 W. Shockley and H. J. Queisser, *J. Appl. Phys.*, 1961, **32**, 510–519.
79 L. Yu and A. Zunger, *Phys. Rev. Lett.*, 2012, **108**, 068701.
80 M. Bernardi, M. Palummo and J. C. Grossman, *Nano Lett.*, 2013, **13**, 3664.
81 A. Standard, *Ann. Book of ASTM Standards 2003*, 2012, vol. 14, pp. 1–20.
82 E. A. Moujaes and A. C. Dias, *J. Phys. Chem. Solids*, 2023, **182**, 111573.
83 D. Jariwala, A. R. Davoyan, J. Wong and H. A. Atwater, *ACS Photonics*, 2017, **4**, 2962–2970.
84 H. J. Goldsmid, *et al.*, *Introduction to thermoelectricity*, Springer, 2010, vol. 121.
85 G. J. Snyder and E. S. Toberer, *Nat. Mater.*, 2008, **7**, 105–114.
86 S. Harris, *An introduction to the theory of the Boltzmann equation*, Courier Corporation, 2004.
87 W. Jones and N. H. March, *Theoretical solid state physics*, Courier Corporation, 1985, vol. 35.
88 A. Togo, L. Chaput and I. Tanaka, *Phys. Rev. B: Condens. Matter Mater. Phys.*, 2015, **91**, 094306.
89 A. Togo, L. Chaput, T. Tadano and I. Tanaka, *J. Phys.: Condens. Matter*, 2023, **35**, 353001.
90 D. T. Morelli and G. A. Slack, *High thermal conductivity materials*, Springer, 2006, pp. 37–68.
91 G. A. Slack, *Phys. Rev.*, 1965, **139**, A507.
92 G. A. Slack, *J. Phys. Chem. Solids*, 1973, **34**, 321–335.
93 D. Raval, E. A. Moujaes, S. K. Gupta and P. Gajjar, *J. Phys. Chem. Solids*, 2024, 112157.
94 D. Sanditov, V. Mantatov, M. Darmaev and B. Sanditov, *Tech. Phys.*, 2009, **54**, 385–388.
95 B. Peng, H. Zhang, H. Shao, Y. Xu, X. Zhang and H. Zhu, *RSC Adv.*, 2016, **6**, 5767–5773.
96 C. L. Julian, *Phys. Rev.*, 1965, **137**, A128.
97 G. Qin, A. Huang, Y. Liu, H. Wang, Z. Qin, X. Jiang, J. Zhao, J. Hu and M. Hu, *Mater. Adv.*, 2022, **3**, 6826–6830.
98 M. Jakhar, P. Chauhan, A. Kumar and R. Pandey, *2D Mater.*, 2024, **12**, 013001.
99 P. Chauhan, J. Singh and A. Kumar, *J. Mater. Chem. A*, 2024, **12**, 16129–16142.
100 N. Verma, P. Chauhan and A. Kumar, *Nanoscale*, 2024, **16**, 14418–14432.
101 R. v. Mises, *J. Appl. Math. Mech.*, 1928, **8**, 161–185.
102 M. L. Pereira Junior, L. A. Ribeiro Junior, W. H. Brandão, A. L. Aguiar, D. S. Galvão and J. M. De Sousa, *ChemPhysChem*, 2020, **21**, 1918–1924.
103 M. L. P. Júnior and L. A. R. Júnior, *FlatChem*, 2020, **24**, 100196.
104 M. Pereira, W. Da Cunha, R. De Sousa, G. A. Nze, D. Galvão and L. Ribeiro, *Nanoscale*, 2022, **14**, 3200–3211.